

58×62 Si:As IBC Detector Arrays on PMOS Multiplexers for Astronomy

M. E. McKelvey, Robert E. McMurray, Jr., C. R. McCreight, T. L. Roellig
NASA Ames Research Center, Moffett Field, CA 94035-1000

R. Cooper, L. Yuen
Orion TechnoScience, Palo Alto, CA 94306

L. K. Deutsch
University of California, Berkeley, CA 94720

ABSTRACT

Four 58×62-element Si:As impurity-band-conduction (IBC) detector arrays produced by the Hughes Technology Center were tested to evaluate their usefulness for space- and ground-based astronomical observations. PMOS circuitry was used in the multiplexers to improve low-temperature noise performance. Laboratory tests at background levels simulating those expected on space-based observing platforms were combined with ground-based telescope IR observations. The devices have shown read noise levels below 120 rms e⁻, dark currents below 10 e⁻/s, and detective quantum efficiencies of 20%.

1. INTRODUCTION

An on-going NASA technology development program over the last several years has sought to advance IR detector and cryo-cooler technology for space-based astronomy¹. Proposed space-borne systems such as the Space Infrared Telescope Facility (SIRTF)² present tremendous challenges for focal-plane-array (FPA) technology because any sort of excess FPA noise will degrade measurements in the minimal infrared backgrounds associated with a cooled orbiting telescope. FPAs capable of achieving background-limited performance in reasonable integration times will be limited to a few rms electrons of read noise in such observations. Because the IR backgrounds are so small, and because the detector materials used in the wavelength range of interest require it, the detector readout must operate reliably and without excess noise at temperatures below 10K.

A number of NASA-funded FPA projects³ have been conducted with the aim of developing cryogenic IRFPAs that approach the kind of low-noise performance obtained with higher operating temperature readouts, such as buried channel CCDs⁴. Impurity-band-conduction (IBC) detector substrates mated to cryogenic charge-integrating switched-FET readout multiplexers represent the state of the art for FPA sensitivity in the 10μm - 30μm wavelength range.⁵ IBC detector substrates promise less sensitivity to the radiation environment and fewer anomalous performance effects than alternative bulk-photoconductor architectures. Switched-FET readouts have been under development for a number of years and have matured considerably, nearing the stringent read noise requirements of space-based astronomy with low power dissipation and good producibility.

The devices described here were produced under contract by Hughes Technology Center in Carlsbad, CA, to determine how closely the state of the art meets the needs of astronomers using space-based telescopes. These devices are near relatives of the Hughes CRC-228 family of 58×62 IRFPAs that have been in use in a number of laboratories and ground-based observatories since 1986.⁶ A considerable body of performance data exists on CRC-228-based devices using various photoconductive and photovoltaic detector substrates. Comparison with this data can help determine whether the present devices represent significant progress in technology development.

2. DEVICE DESCRIPTION

The multiplexer is essentially a PMOS implementation of the CRC-228, with the addition of diode protection on all inputs and an option to bypass the two large output transistors, giving direct access to the first stage unit-cell source-follower. Like the CRC-228, this design makes use of direct read-out source follower per detector (SFD) architecture with nondestructive read capability and optional signal reset, for use in many different sampling modes. Seven row and seven column address lines provide random access to the unit cells to allow a variety of clocking schemes. This allows, as an example, for different

integration times over different areas of the array. This might prove useful should a single field of view contain sources of widely differing intensities. Areas of the array imaging bright sources could be reset more often to prevent saturation, while the rest of the array could perform a deeper integration to pull out fainter sources.

A schematic diagram of the multiplexer is shown in Figure 1. The pixel pitch is $76\text{ }\mu\text{m}$, allowing the utilization of four transistors per unit cell with relaxed design rules. Each unit cell carries two detectors (designated “even” and “odd”), so that each valid address selects two pixels. Three of the seven row address lines are activated to select a particular row, connecting each pixel of that row with an active load FET to complete the first stage source-follower circuit. The 62 active load FETs serve to set the operating point on the output transfer function and are found to be the dominant factor in device power dissipation. Three of the seven column address lines are activated to connect the source-follower of a particular unit cell to the output source follower. A reset line can be activated during a valid address to reset the integration node, beginning a new integration. A number of “non-destructive” reads of pixel signal can be obtained by choosing not to activate the reset line.

A combination of capacitances at the node connecting the detector, reset switch, and source-follower input gate is used to store photogenerated charge during integration. The major contributors to this “sense node” capacitance are the MOSFET gate oxide capacitance (approximately 0.3 pF) and the capacitance associated with the depletion width in the IR-active detector layer.

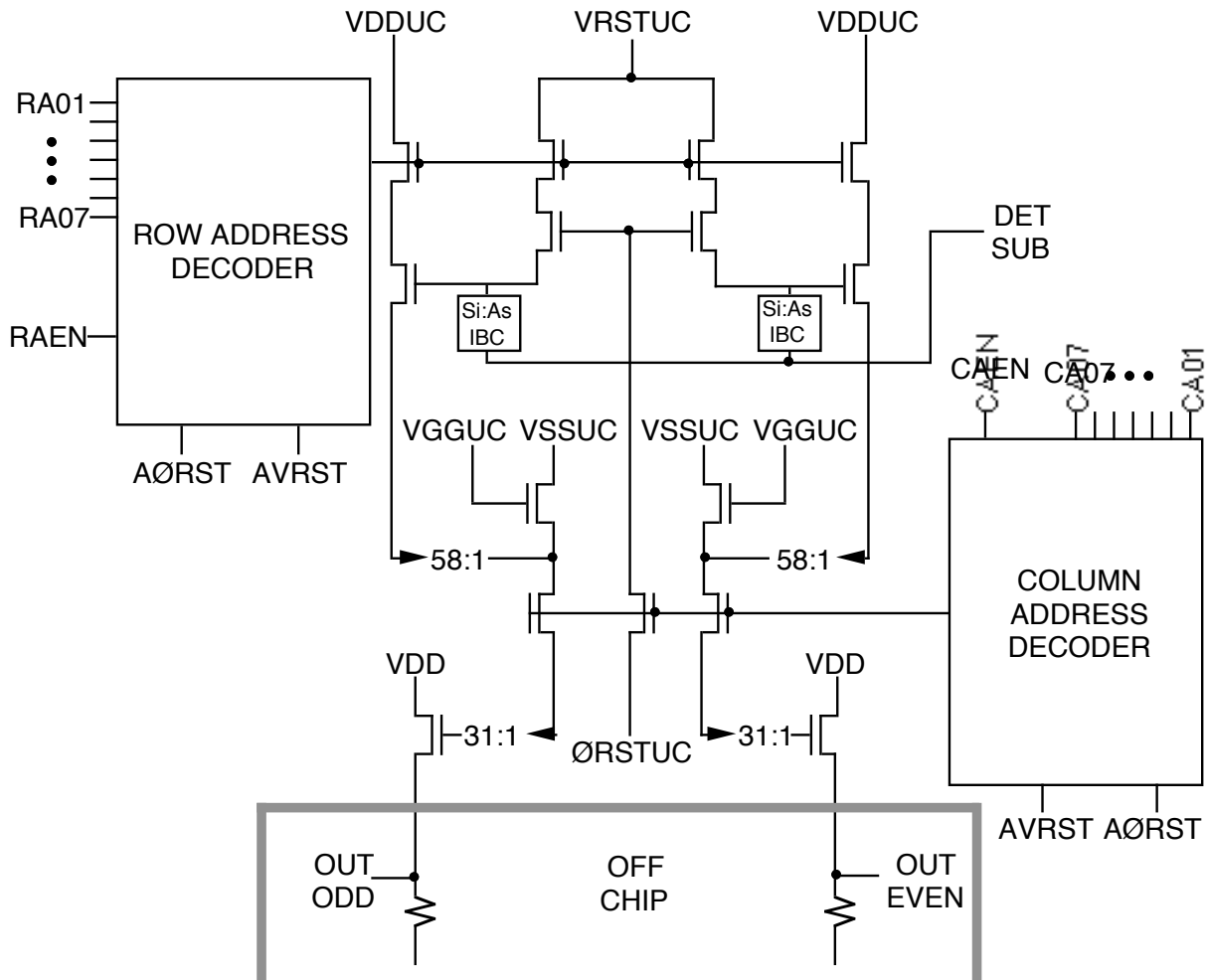


Figure 1. Reduced schematic of the 58x62 address decoding and unit cell.

The 58 \times 62 readouts were grown on the same wafers as the CRC-644 256 \times 256 Hughes readouts. The 256 \times 256 devices are the subject of another paper in this volume⁷, wherein more details of the process can be found. All the subject 58 \times 62 readouts come from the “HTC Standard Cryo-CMOS” process splits, and not from the newer experimental ultra-low noise process.

The detector substrate is a backside-illuminated arsenic-doped-silicon (Si:As) IBC structure with 76 μm square pixels and a 20 μm thick epitaxially grown IR active layer doped to an As concentration of $5 \times 10^{17} \text{ cm}^{-3}$. A common transparent “blanket” contact is implanted at the active layer/substrate interface to supply the detector bias voltage. The magnitude of the bias field is set by the difference between the reference potential (*VRSTUC*) and the potential at the transparent contact (*DETSUB*).

3. EXPERIMENTAL OBSERVATIONS

Measurements were made at Ames Research Center on four of the eight delivered devices. Devices were mounted in turn in a low-background liquid helium test dewar equipped with a cold filter wheel, viewing an external blackbody source through a KRS-5 window with an f/180 beam. A dedicated VME rack containing a single-board 68020 computer and a 12-bit analog-to-digital converter, drives the array and coadds the output signals. The VME rack connects via ethernet to the host computer that runs the user interface and performs display and data processing functions.

Multiplexer-specific electrical testing was performed to verify proper connection and basic functionality. Basic tests on multiplexer source-follower characteristics were performed next, followed by more detailed determination of several basic figures of merit for the hybrid device. Highlights of the results are contained in Table 1. Except as noted in the table, the summary results represent performance under a set of nominal operating conditions found to give good performance, rather than absolute best performance in any one category.

Table 1. 58 \times 62 Si:As IBC Performance Summary.

Characteristic	Units		Comments
<u>General</u>			
Material	Si:As		
Format	58x62		
Pixel pitch	75	μm	
Wavelength range	6-28	μm	
<u>Measurements</u>			
Read Noise	110	e ⁻	6K, -1.6V bias, low q _b
Dark Current	<10	e ⁻ /s	5.5K, -2V bias
G□	0.6		4.6K, -2Vbias, 22μm
	2.0		-3Vbias, near breakdown
Detective Q. E. (□/□)	20	%	
Input capacitance	.12	pF	
Well capacity	>6x10 ⁵	e ⁻	Transfer function limited
Max. Integration time	>5x10 ⁴	s	I _d limited
Operating temperature	5-8	K	
Operable pixels	>99	%	

Source-Follower Operation

Operation of the source-follower-per-detector amplifier is crucial in the determination of the gain, linearity, well capacity, and power dissipation of the hybrid device. Ideally, the source-follower will provide a wide, linear dynamic range with high frequency bandwidth at low currents (for minimal power dissipation). Linear range is largely set by the values of the source and drain voltages supplied to the multiplexer and source resistance. Some earlier NMOS versions of this readout studied under this program suffered from a “kinking” non-linearity in the transfer function. The kink arose when the difference between the source-follower “rail” voltages was increased beyond nominal values in attempts to increase the linear range. Field-induced impact ionization in the source or drain region of one of the FETs is believed to be responsible for this behavior. The kinking behavior was not observed on the later PMOS versions of the readout.

Figure 2 shows the transfer function and the corresponding output FET drain current at the operating point recommended by Hughes for one of the PMOS devices. The top rail is set by the 9 V setting of VSS. The bottom rail is set by either the lower limit of the transistors used as switches to pass potentials into the sense node or by an insufficient drain-source voltage across one of the source-follower FETs. With a source resistance of 33 k Ω , a linear gain of 0.75 is observed for VRSTUC values between 5.4 V and 6.2 V at this operating point. Power dissipation is small ($< 1 \text{ mW}$). With the measured input

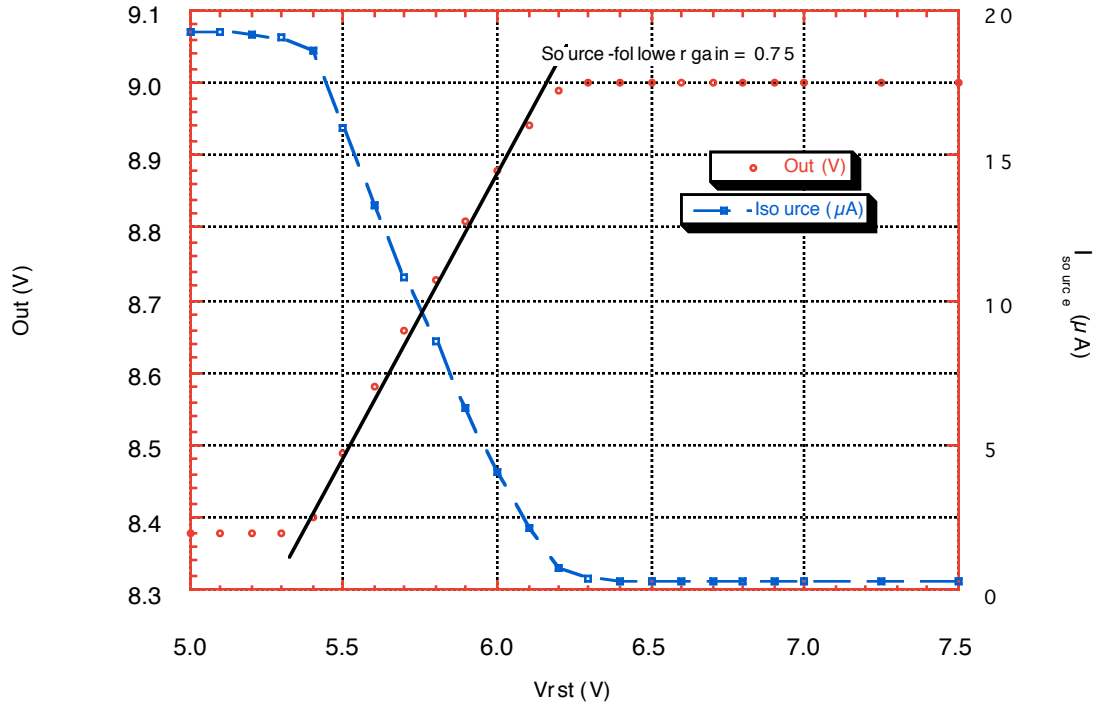


Figure 2. Transfer function and output driver current vs. sense node potential.
 $T = 4.6\text{ K}$. $VSS = VSSUC = 9\text{ V}$. $VDD = VDDUC = 6.5\text{ V}$. $VGGUC = 7.6\text{ V}$.

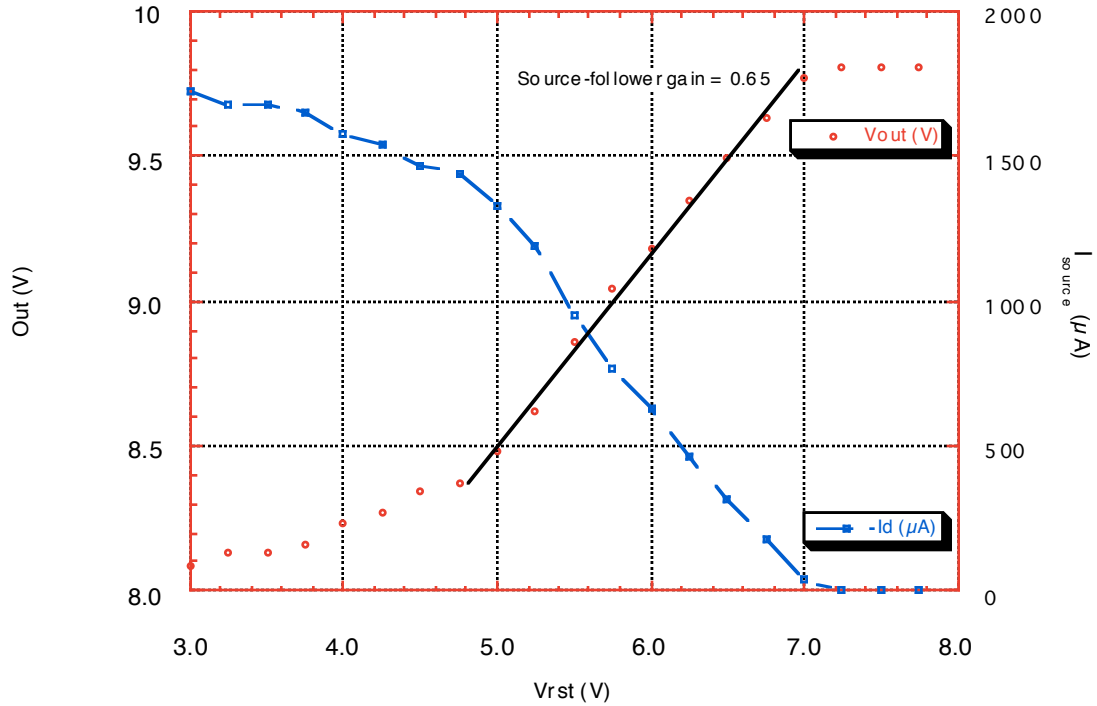


Figure 3. Transfer function and output driver current vs. sense node potential.
 $T = 10.0\text{ K}$. $VSS = VSSUC = 9.9\text{ V}$. $VDD = VDDUC = 5.0\text{ V}$. $VGGUC = 8.0\text{ V}$.

capacitance, this translates to a transfer-function-limited well capacity of 5.7×10^5 electrons. This is a good-sized well for low background work, but ground-based astronomy requires the capability to accommodate large background levels.

Figure 3 shows a plot analogous to Figure 2, but with the operating point changed to better cope with atmospheric 10^4 m backgrounds. A $1\text{ k}\Omega$ source resistor is substituted to increase the bandwidth for higher frame rates. The source-follower rails are moved to 9.9 V for sources and 5.0 V for drains. The result is a higher maximum frame rate ($> 200\text{ Hz}$), much higher current in the output driver FET resulting in an increase in focal plane temperature (to nearly 10 K with existing heat sinking), a lower source-follower gain, and an increased linear range of 4.8 V to 7 V on the sense node, free of “kinks” in the transfer function. This corresponds to a transfer-function-limited well capacity of about 1.6×10^6 electrons.

At the operating point of Figure 3, the photon-signal-dependent current through the source follower is large enough to affect the equilibrium temperature of the device, and thus the power dissipation in the device becomes significantly flux-dependent. Currents in the output driver as large as 1 mA are large enough to cause either local heating or “glow” that would degrade device uniformity, and the increased temperature would cause unwanted dark current. For these reasons the operating point of Figure 3 is not suitable for space-based low background astronomy, and Figure 2 is more representative of device performance in such applications.

Stability

Tests were performed to characterize the stability of the array over long periods of time to help determine how often recalibrations are necessary in astronomical observations. Drift in the correlated-double-sampled (CDS) signal was measured over 2.5 h with the photon flux blanked off. The results are shown in Figure 4. Device temperature was 5.5 K, and the bias voltage was -1.5 V. The standard deviation from the mean over 2.5 h was $31\text{ }\mu\text{V}$, equivalent to about 30 electrons at the sense node. With the measured read noise of 110 e^- , drift in the output is not a significant problem.

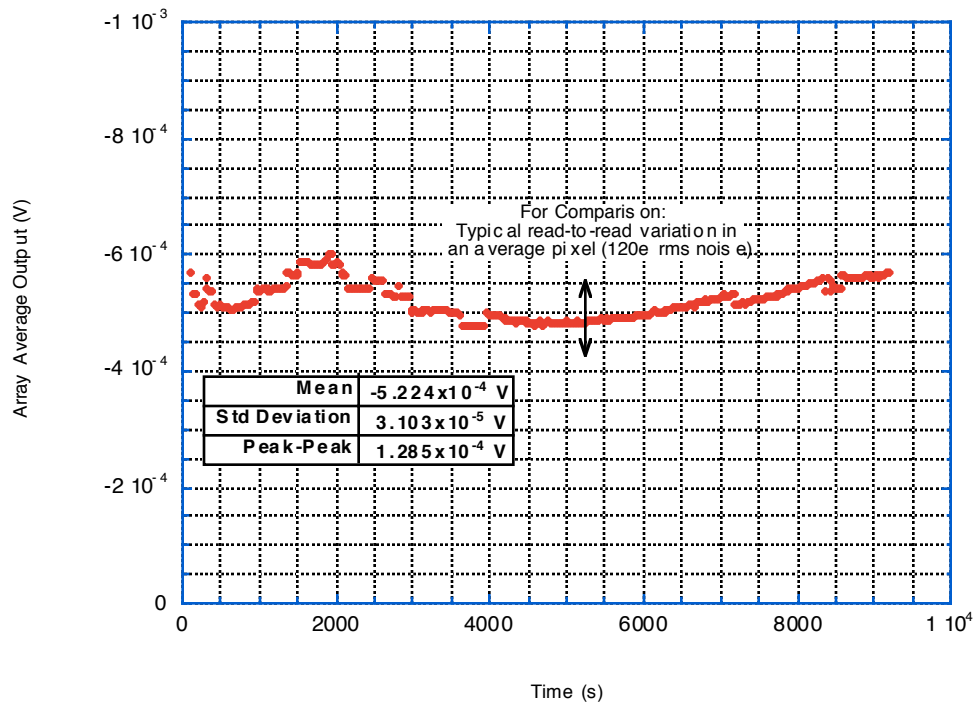


Figure 4. Array average signal drift. All pixels averaged. CDS signal referred to array output. $T = 5.5\text{ K}$.

While array CDS signal stability over time was good, two of the devices tested (serial numbers NA056 and NA053) show output waveform instability. Under some circumstances these parts spontaneously develop long time constants in source-follower output after about 30 min of continuous operation. The time constants can become so long that the signal, reset, and pedestal levels do not settle within the time available at reasonable frame rates. The long time constants can be

eliminated by cycling the clock line power supplies off and on again, but they persist through a thermal anneal to 15 K. This suggests that the problem may be related to charge distribution in the readout. Information so far is not definitive, but it appears that the conditions for the onset of the instability may depend on temperature and perhaps on flux levels. Two other devices tested at ARC have not shown this problem. Tests at the University of Arizona have shown similar problems on individual transistors from Hughes process monitors. This behavior is under further study.

Input Capacitance

Measurements of array reset current and output signal were made at various IR flux and bias voltage levels. Plots of current vs. output signal yield the input capacitance as part of the proportionality constant. Figure 5 is a plot of these measurements. Signal from all pixels in the array is averaged, and in this case are referred to the preamplifier output. Reset current was measured with a slow-reacting ammeter placed in the reset line.

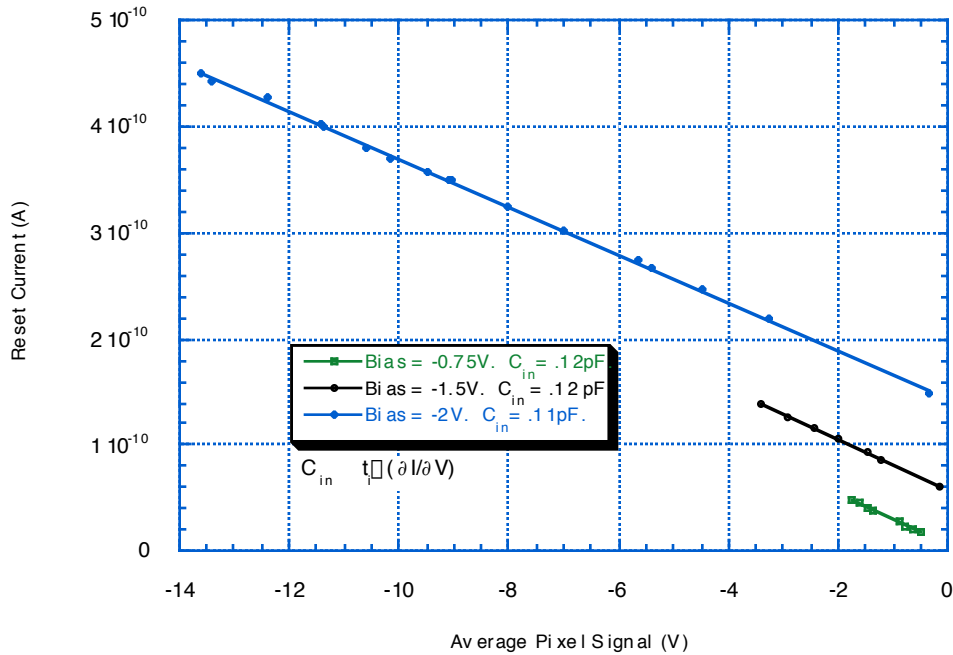


Figure 5. Reset current as a function of average pixel signal. Signal is preamp-output-referred. Temperature = 8 K. Integration time = 233 ms.

The 200Å thick oxide should have a capacitance near 0.3 pF, and this should add directly to the bias-dependent capacitance of the depletion in the IR-active layer. The depletion capacitance is expected to be about

$$C_{\text{det}} = C_o \frac{d}{dI/dV(V)}$$

where C_o is the expected capacitance of the blocking layer only, d is the blocking layer thickness and $w(V)$ is the depletion width in the IR active layer. Calculations of $w(V)$ based on reasonable estimates of compensation in the active layer would lead to $C_{\text{det}} \approx .14 \text{ pF}$ at 0 bias, dropping to about .02 pF when the active layer is fully depleted.

Effective input capacitance was found to be near 0.1 pF at each bias level tested. This value is significantly lower than even the calculated capacitance of the integrating FET gate oxide alone, suggesting that some of this capacitance may be shielded by channel modulation associated with the action of the source follower. No bias dependence in the input capacitance was

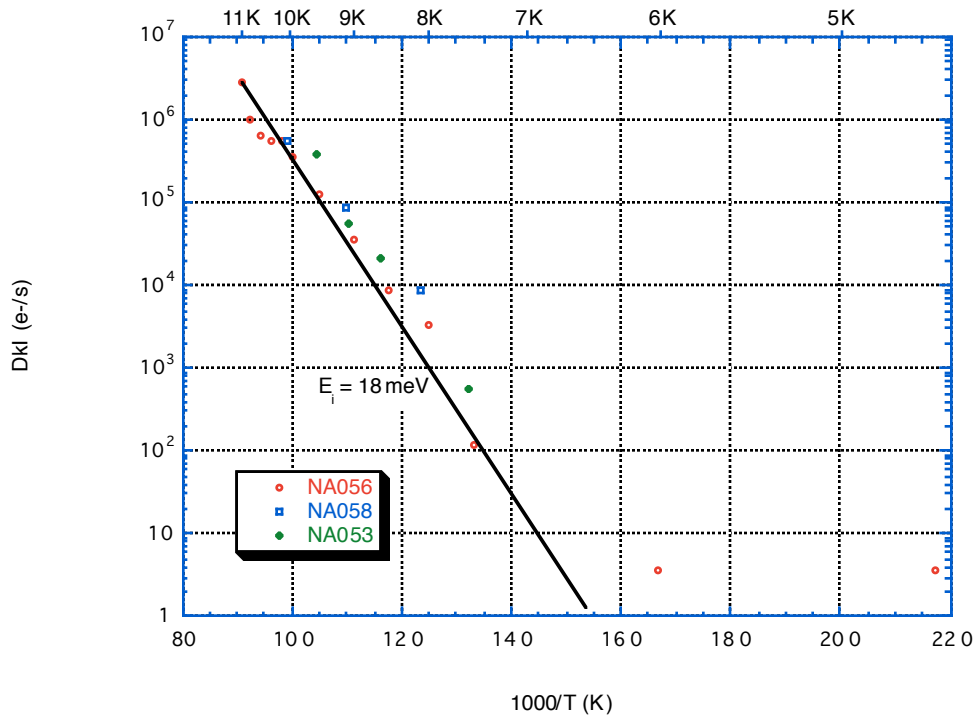


Figure 6. Dark current as a function of $1000/T$.

observed, which may suggest that we are nearly fully depleted even at 0.75 V applied bias since the detector capacitance drops quickly as the depletion width grows. Measurements of quantum efficiency described below are consistent with an active layer that is fully depleted even at moderate biases.

Dark Current

Dark current measurements were made on three of the delivered devices, and all showed similar results. Our test station was eventually found to have a low-level light leak, which was repaired after the dark current tests were done on two of the parts. Consequently, only one of the parts (serial number NA056) was measured in the darkest test dewar configuration. All parts tested showed comparable results above the light-leak limit, therefore it is reasonable to expect that all parts tested would show dark currents as low as NA056 if tested in the same dewar configuration.

Array average signal was measured at various integration times, temperatures, and bias voltages. For a particular bias and temperature, signal was plotted against integration time. The slope of a best-linefit to the data yields the dark current. The results from a number of these tests are contained in the Arrhenius plot of Figure 6. In general the dark currents measured were very low. Although measurements of the smallest dark currents are very difficult, values above 10^{-4} e-/s are detectable in our test system. At lower levels, our signal vs. integration time measurements are limited by drift in the electronics. Thus the lowest dark currents in the plots are estimates obtained from (poor) linear fits to the drift-limited data, and could equally well be described as too low to measure with our equipment.

Dark current in all devices tested rose sharply as temperatures increased above 7 K, with an activation energy near 18 meV. The observed activation energy is typical of Si:As IBC devices tested at Ames.

Serial number NA056, the device on which the lowest dark currents were measured, showed a number of anomalies at long integration times. Under some circumstances it showed a fair number (50-100) of pixels that began to leak badly over time. These leaky pixels could be recovered by cycling power to the clock lines, and the phenomenon may be related to the waveform instability described above. A “bright” corner was also observed, presumably due to localized warming or glow from some component in the mux. In order to measure the underlying dark current prevalent in the device, these bright areas

and leaky pixels were masked in the low dark current data shown. There are >2000 unmasked pixels averaged in all the data shown here.

Response and Noise

Measurements of response were made using IR flux from an external blackbody source. A $22\ \mu\text{m}$ narrow-band filter and a 1.3% neutral density filter were placed in the f/180 beam to limit the background level to $2 \times 10^5\ \text{ph/pix-s}$ with 295K in the field of view.

The photo-gain/quantum efficiency product ($G\%$) shows a weak dependence on temperature, dropping by about 15% between 5K and 7K (closed dots in Figure 7). At this background level and integration time photon noise dominates over read noise, although there is a noticeable increase in read noise at the lowest temperatures. Refinements to the test setup after the data in Fig. 7 were taken have resulted in improved noise performance; the read-noise-only line in Figure 7 would be 10-20% lower if the data were re-taken with the improved system. At present, noise sources other than the device under test have not been ruled out as limiting contributors to measured noise. Efforts continue to eliminate any excess noise sources.

The data in Figure 7 were obtained at non-optimum bias; the detective quantum efficiency at this operating point is calculated to be 7-10 %. The temperature-dependence of responsivity has not yet been measured at other bias levels.

Figure 8 shows calculated $G\%$ and detective quantum efficiency as functions of applied bias. In other reported tests of IBC detectors, the $G\%$ vs. bias curve shows a flat region at intermediate bias voltages. The flat region is thought to correspond to bias voltages sufficient to fully deplete the IR-active layer but insufficient to cause the high photo-gains characteristic of high biases. Data taken on the present devices do not show such a flat region. This is consistent with other indications (mentioned above) that the active layer may be fully depleted even at small applied bias. Note that a small applied bias may represent a substantial *effective* bias when clocking-induced capacitive feedthrough onto the sense node is taken into account

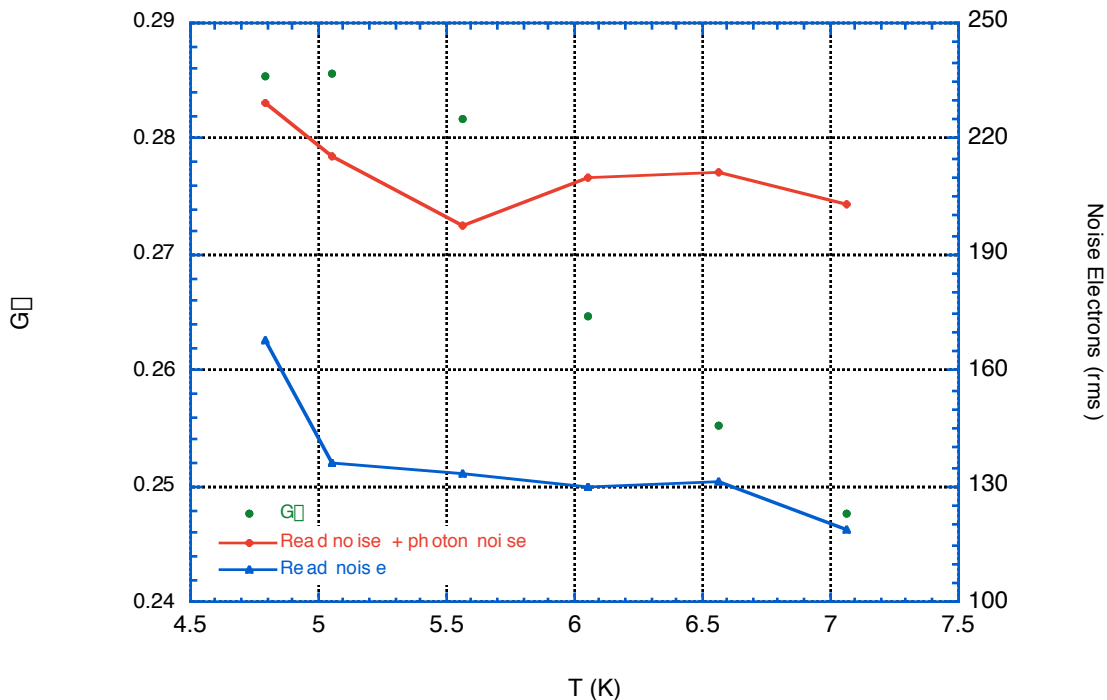


Figure 7. Temperature dependence of response and noise. Bias = -1.5 V.
Integration time = 233 ms. Background = $2 \times 10^5\ \text{ph/pix-s}$.

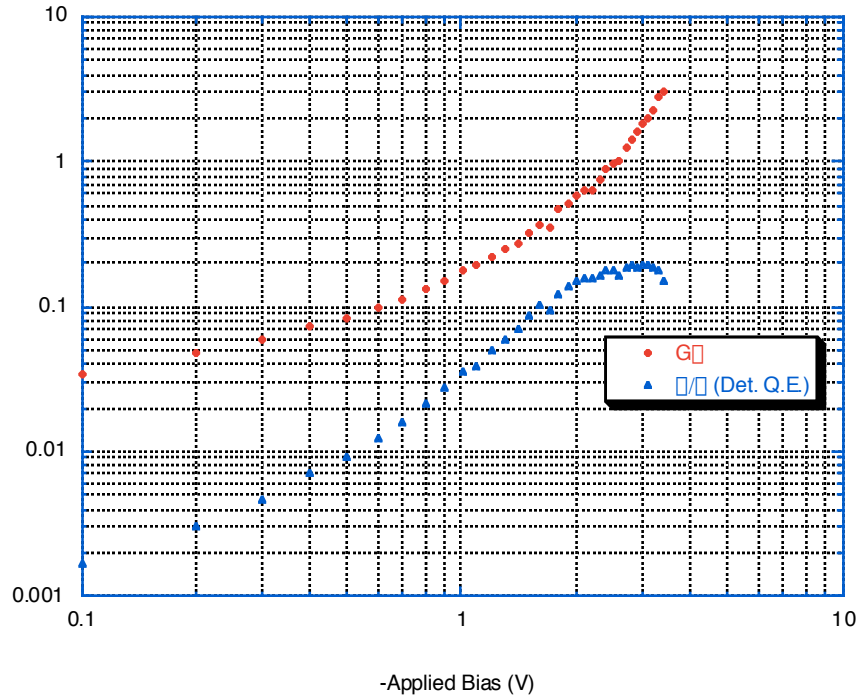


Figure 8. Response, detective quantum efficiency as a function of applied bias voltage. $T = 4.6$ K. Integration time = 233 ms.

(the actual zero-response point corresponds to an applied bias of +0.5 V to +1.0 V). Measured G compares well with Hughes' measurements at similar applied bias voltages.

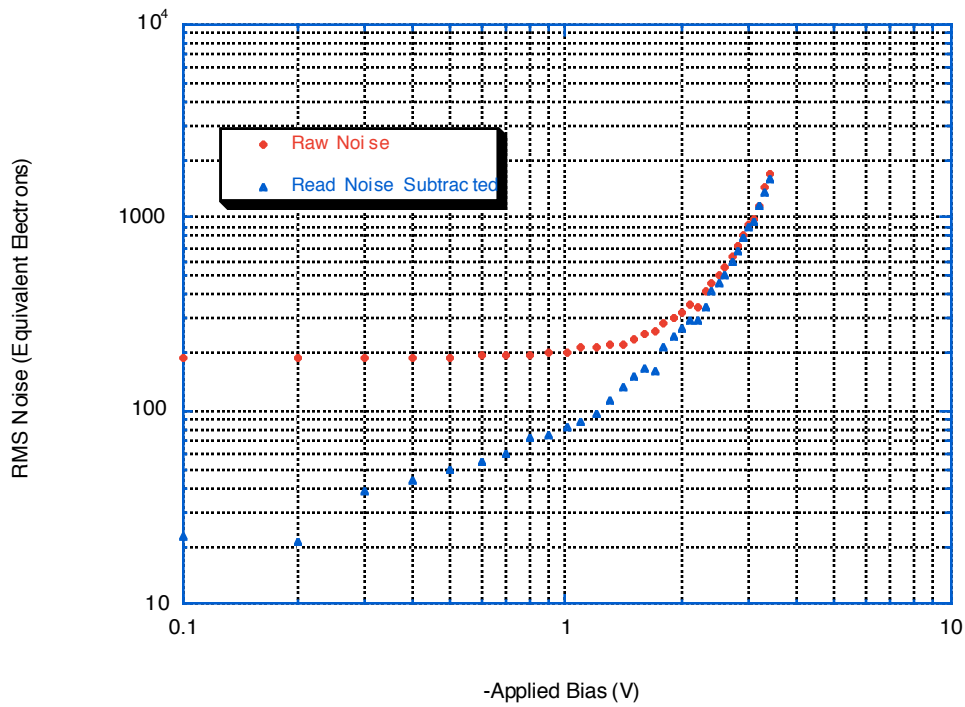


Figure 9. Bias dependence of noise. Diamond symbols represent total noise, including read noise and photon noise. Triangles represent noise with the dark read noise removed in quadrature, approximating the read noise contribution.

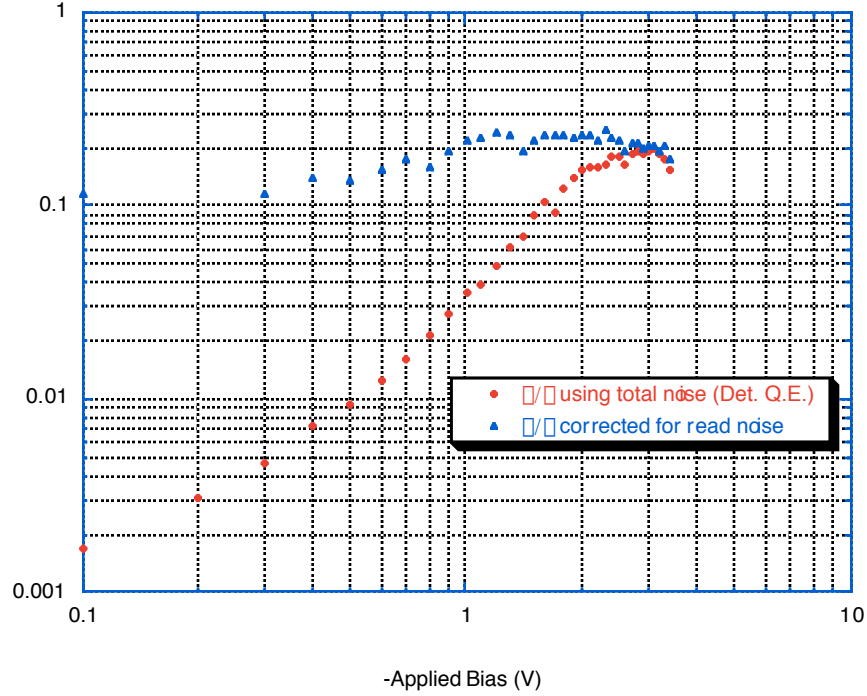


Figure 10. Detective quantum efficiency corrected for excess read noise.

The detective quantum efficiency (also called \square/\square , though $DQE = \square/\square$ only in the absence of excess noise sources) is determined through the square of the ratio of the observed signal-to-noise ratio (SNR) to the background-limited SNR. The calculation rests on the assumption that the ideal, photon-limited SNR is equivalent to the square root of the integrated flux (Poisson statistics). In Figure 8, DQE is flat between 2V and 3V applied bias at about 20%. At higher biases, noise goes up (probably due to impact ionization and a corresponding increase in the gain dispersion \square) and DQE goes down. At lower biases excess read noise and possibly a less-than-fully depleted IR active layer combine to reduce DQE.

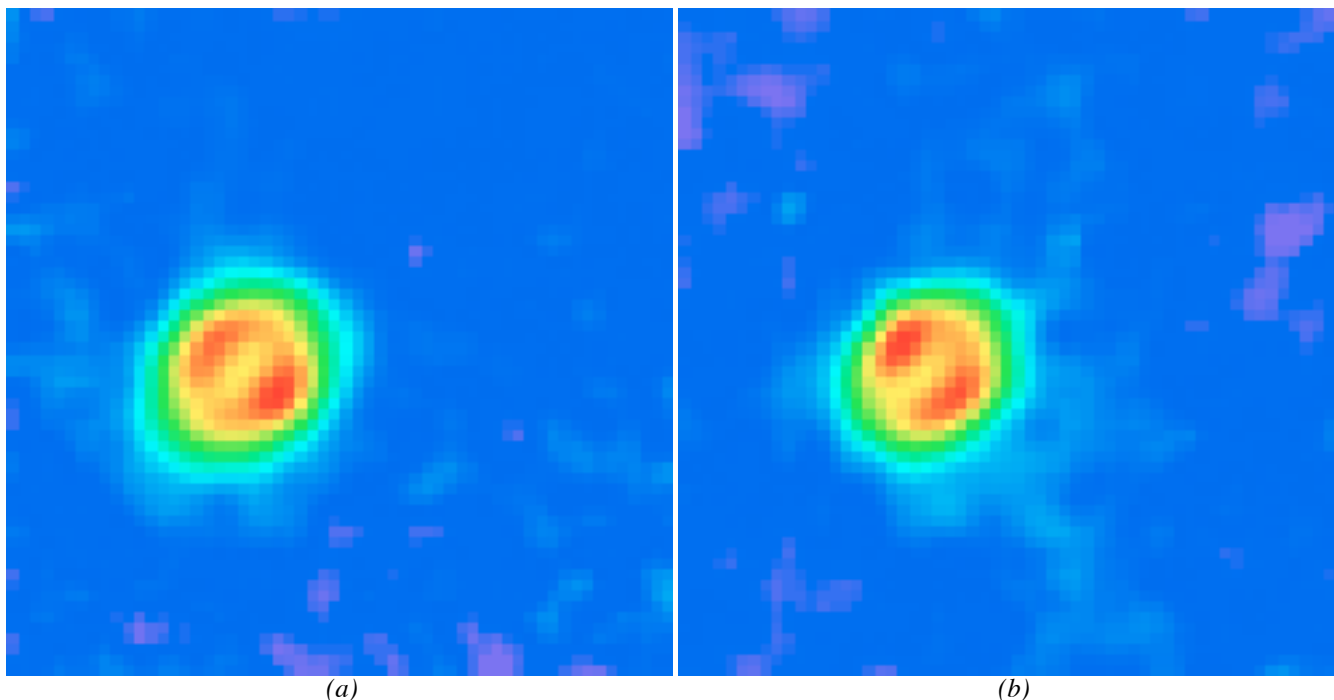
Read noise dominates noise performance at low biases because responsivity is low. A better look at \square/\square may be obtained by removing in quadrature the excess noise, measured in the absence of photon flux. Figure 9 shows the noise measured in the presence of photon flux (diamond symbols) along with the estimated contribution to this noise from photon noise only (triangles). The photon noise estimate is obtained by subtracting from the total in quadrature a dark measurement of read noise vs. bias.

The resulting estimate of photon noise can be used in a recalculation of SNR, and in turn in a recalculation of detective quantum efficiency. The result is plotted in Figure 10, along with the calculated DQE using the total noise (as in Figure 9) for comparison. With the read noise subtracted, \square/\square is relatively flat down to about 1V bias.

4. ASTRONOMY DEMONSTRATION

T. Roellig has led the development at Ames of a new infrared camera incorporating these detector arrays for observations from ground-based telescopes. The camera is designed for use in both the 10 and 20 micron atmospheric windows. Three discrete 8% filters at 18, 20, and 22 microns, as well as a 3% circular variable filter covering the 7.5-14 micron wavelength range, define the spectral resolution. Flexible optical design and a dedicated guider/mounting box allow camera operation at any major telescope that has a F/# ratio of 17 to 45. The camera is still undergoing development, but has been used on two engineering observing runs at the Mt. Lemmon 60-inch telescope in November 1992 and February 1993.

The camera was found to meet all of its designed sensitivity performance goals during the two observing runs. On the 60-inch Mt. Lemmon telescope, the camera sensitivity was found to be 0.08 Janskys/pixel in one minute of telescope observing



(a) (b)
Figure 11. Images of NGC 7027 at 11.4 μm (a) and 10.4 μm (b) with an 0.33 μm spectral bandwidth taken with the Ames Mid-Infrared Camera using the 60-inch telescope on Mt. Lemmon.

time, which translates into a diffraction-limited point-source sensitivity of 0.04 Janskys in one minute of telescope observing time. Each camera pixel corresponded to a square 0.73 arc-seconds wide on the sky, which gave a total camera field-of-view of 42 x 45 arc-seconds. Examples of images taken during the first engineering run are shown in Figures 11(a) and 11(b). These figures show images of the planetary nebula NGC 7027 at two wavelengths, with higher flux levels indicated by progressively lighter shades and lower flux levels indicated by progressively darker shades. In these figures, North is to the top and East is to the left. The infrared image size of NGC 7027 is approximately 15 arc-seconds by 12 arc-seconds in both figures. These images clearly show the two-lobed structure of NGC 7027 in the infrared. The images also show that the shape of the object does not change between 10.4 and 11.4 microns. This is important, because the 10.4 micron flux arises solely from thermal emission from warm dust grains, while the 11.4 micron flux also has a component arising from a line emission feature centered at 11.3 microns.

Now that the camera is working well, additional engineering test observations on the Mt. Lemmon telescope will be used to verify the performance of its polarimetric capabilities. Future plans also include taking the Ames IR camera to larger telescopes on Mauna Kea in Hawaii, where it will be used in studies of interacting galaxies and particle shells around stars.

5. SUMMARY

A new generation of Hughes CRC-228-based detector arrays has been evaluated to determine and to demonstrate their usefulness in astronomical applications. Results to date include verification of most of the figures of merit claimed made by Hughes for these devices. Dark current and read noise measurements gave results significantly better than claimed by the manufacturer. Device operability, responsivity, multiplexer functionality and stability were demonstrated at a high level of performance. A detective quantum efficiency of 20% was demonstrated.

Development and use of a mid-infrared camera built around this device has shown that real astronomical observations can be made with these arrays with performance similar to that obtained in laboratory tests. The camera has so far met all of its designed sensitivity goals, with good imaging properties and operability.

Noise performance in the laboratory tests described may not represent the ultimate noise floor of the device. Further refinement of the amplifiers and bias voltage supplies in the test system may result in even higher sensitivity. Future work with these and other Hughes IBC arrays will determine how well the present state of the art as implemented at Hughes approaches the sensitivity required for space-based astronomy.

6. ACKNOWLEDGMENT

This work was supported by Dr. M. Sokoloski and the Office of Aeronautics and Space Technology, NASA Headquarters, Washington D. C. We wish to thank Dr. Donald Jennings of GSFC for the loan of one of the devices tested. J. Asbrock, N. Lum, R. Kelchner and R. White of the Hughes Aircraft Company Technology Center provided valuable insight and discussion.

7. REFERENCES

¹McCreight, C. R. and Wilson, B. A., "Future astronomical infrared detector needs for space astronomy," Infrared and Millimeter Wave Engineering, Hal Busher, Ed., Proc. SPIE Vol. 1874-37, 1993.

²Werner, M. W., "Scientific goals of the SIRTf Mission," Infrared and Millimeter Wave Engineering, Hal Busher, Ed., Proc. SPIE Vol. 1874-28, 1993.

³See for example: McMurray, Robert E., Jr., *et al.*, "256 \times 256 switched-FET multiplexer for spaceborne astronomical applications," Proc. SPIE 1684, 40, 1992, or McKelvey, Mark E., *et al.*, "Laboratory Characterization of Direct Readout Si:Sb and Si:Ga Infrared Detector Arrays," Proceedings of the Third Ames Infrared Detector Workshop, NASA TM-102,209, pp. 403-412, 1989.

⁴Janesick, J.R., Elliot, T., Collins, S. Marsh, H., Blouke, M., and Freeman, J., "The Future Scientific CCD," Proc. SPIE 501, 2, 1984.

⁵Bothwell, M., "Infrared detector development for future space astrophysics missions," Infrared and Millimeter Wave Engineering, Hal Busher, Ed., Proc. SPIE Vol. 1874-43, 1993.

⁶See for example: W. J. Forrest, *et al.*, "Infrared Array Development for the SIRTf Infrared Array Camera (IRAC)," Bull. Am. Astron. Soc. 20, 1004, 1989; Fowler, A., *et al.*, "The NOAO Infrared Imagers: Description and Performance," Infrared Astronomy With Arrays, C.G.Wynn-Williams and E.E.Becklin editors, pp.197-203, Hilo, Hawaii, 1987; or McLean, I. S., *et al.*, "Experience with the UKIRT InSb Array Camera," Proceedings of the Third Ames Infrared Detector Workshop, NASA TM-102,209, pp. 183-200, 1989.

⁷Lum, N. A. *et al.*, "Low-noise 256 \times 256 Staring FPA", Proc. SPIE Vol. 1946-13, Orlando, FL, 1993.